Full-scale identification of the wave forces exerted on a floating bridge using inverse methods and directional wave spectrum estimation

Petersen, Øyvind Wiig; Øiseth, Ole; Lourens, Eliz-Mari

DOI
10.1016/j.ymssp.2018.10.040

Publication date
2019

Document Version
Accepted author manuscript

Published in
Mechanical Systems and Signal Processing

Full-scale identification of the wave forces exerted on a floating bridge using inverse methods and directional wave spectrum estimation

Ø.W. Petersen[a,*], O. Øiseth[a], E. Lourens[b]

[a]*NTNU, Norwegian University of Science and Technology, 7491 Trondheim, Norway*
[b]*Delft University of Technology, 2628 CN Delft, The Netherlands*

Abstract

The dynamic behaviour of long-span bridges is governed by stochastic loads from typically ambient excitation sources. In real life, these loads cannot be measured directly at full scale. However, inverse methods can be utilised to identify these unknown forces using response measurements together with a numerical model of the relevant structure. This paper presents a case study of full-scale identification of the wave forces on the Bergsøysund bridge, a long-span pontoon bridge that has been monitored since 2013. First, a numerical model of the structure is formed, resulting in a reduced-order state-space model that takes into account the frequency-dependent hydrodynamic mass and damping from the fluid, based on fitting of [..[1]]rational transfer functions. Using acceleration data of the structure measured during several events of moderate and strong seas, the wave forces are identified using stochastic-deterministic methods for combined state and input estimation. In addition, a separate frequency-domain assessment of the wave forces is performed, in which the spectral density of the first-order wave forces is constructed from an estimated directional wave field model driven by wave elevation data. When compared in the frequency domain, the force estimates from the two approaches are of comparable magnitude. However, uncertainties in the assumptions and models behind the force estimates from the two approaches still play a significant role.

Keywords: structural monitoring; wave force; force identification; floating bridge; wave field

1. Introduction

For long-span bridges, a good understanding of the dynamic behaviour is essential to ensure the life-time integrity of these structures. Numerical simulations of the dynamics of long-span bridges have come far, as increased computational power has allowed complex models to be handled in combination with many loading scenarios. However, the numerically obtained response has inherent uncertainties from the structural model and the adopted load model. Models of the ambient loads are dictated by design codes, often supplemented by hindcast data or on-site field measurements for the specific structure prior to construction. The numerical simulations can also be combined with scale model experiments conducted in ocean basin laboratories for marine structures or in wind tunnels for long-span cable-supported bridges. Even though the experiments may allow a good physical representation of the problem, the scaling laws used to design these experiments can introduce additional uncertainties.

*Corresponding author
Email addresses: oyvind.w.petersen@ntnu.no (Ø.W. Petersen), ole.oiseth@ntnu.no (O. Øiseth), e.lourens@tudelft.nl (E. Lourens)
URL: https://www.ntnu.edu/kt/research/dynamics (Ø.W. Petersen)
[1]removed: the

Compared to small-scale experiments, the full-scale monitoring of structures offers the advantage of observing the behaviour under real operational conditions. The input forces on civil engineering structures are, however, impractical to measure directly at full scale. For vibrating structures, the response is far easier to measure, typically by means of accelerometers or strain gauges. This leads to the proposal of force identification techniques, where the idea is to estimate the input forces using the output response data.

Active development and experimental testing of new methods for input estimation have occurred in recent years. Wind load identification by Kalman-filter-based inverse methods has been utilised in wind tunnel tests of chimneys [1] and buildings [2], as well as in field measurements on super-tall buildings [3, 4]. Among the techniques that have gained popularity are the class of Kalman-type methods for combined state and input estimation, for example an augmented Kalman filter [5], a dual Kalman filter [6], and joint input-state estimation algorithms with instantaneous inversion [7, 8] or time-delayed inversion [9]. In experimental and full-scale applications, these methods have also been tested in studies of ice forces on Arctic structures [10, 11].

This article presents an application of a new smoothing algorithm for input estimation [9], where we aim to identify the full-scale wave forces on a long-span floating bridge. The Bergsøysund bridge is a pontoon-type bridge located on the northwest coast of Norway and has been monitored since 2013. These types of floating bridges are currently under consideration in the E39 Coastal Highway Route project for crossing fjords that are several kilometres wide, as conventional bridges are not a viable option. The new designs require a detailed analysis of the response to ambient loads. Numerical studies of the wave-induced response for super-long floating bridge concepts have been performed for homogeneous [12, 13] and inhomogeneous [14] wave conditions. However, the true load conditions may not conform to the numerical load models. In this contribution, we wish to test the practical applicability of the inverse methods for input estimation to a real-life structure. It is well known that the identification of forces at full scale poses a challenge, i.e., facing uncontrollable factors such as noise, model errors and uncertainties.

In floating bridges, the effect of the surrounding fluid plays an important role in the global dynamic behaviour. For linear systems with fluid-structure interaction (FSI) and stationary stochastic loading conditions, frequency-domain studies are common since the fluid effects often are well defined by frequency-dependent transfer functions. In the time domain, these functions appear as convolution terms, which can be difficult to handle efficiently. This article therefore also presents a framework for the linear time-domain modelling of floating bridges. Herein, the convolution terms are replaced with an equivalent state-space model, which is crafted by curve fitting rational transfer functions to the added mass and damping from the fluid. A similar approach has been widely used in marine control applications for vessels and floating structures; see, e.g., [15–17]. Alternatively, one can use time-domain identification methods of state-space models based on impulse responses instead of frequency responses [18, 19].

This paper consists of two main parts. The first covers the equations for the modelling of floating bridges in a finite element (FE) format and, in particular, the establishment of a time-invariant system model. In the second part, the established system model is utilised, together with measurement data from the Bergsøysund bridge, in a force identification study where we assess the wave forces on the pontoons.

2. Time-domain models of the dynamic behaviour of floating structures

This section covers the time-domain modelling of elastic floating structures that are supported at discrete points, e.g., by pontoons. The motion of these structures is governed not only by the structural properties but also by the FSI with the surrounding water at the pontoons.

Let $\mathbf{u} \in \mathbb{R}^{n_{DOF}}$ be the vector containing the n_{DOF} degrees of freedom (DOFs) of the system. When only wave forces are considered, the frequency-domain representation of the equations of motion is given as follows:

$$-\omega^2(\mathbf{M}_s + \mathbf{M}_h(\omega))\mathbf{u}(\omega) + i\omega(\mathbf{C}_s + \mathbf{C}_h(\omega))\mathbf{u}(\omega) + (\mathbf{K}_s + \mathbf{K}_h)\mathbf{u}(\omega) = \mathbf{L}_p\mathbf{p}_w(\omega) \tag{1}$$

Here, $\mathbf{p}_w \in \mathbb{R}^{n_p}$ are the wave forces assigned to the wetted DOFs by the binary selection matrix $\mathbf{L}_p \in \mathbb{R}^{n_{DOF} \times n_p}$. $\mathbf{M}_s, \mathbf{C}_s$ and $\mathbf{K}_s \in \mathbb{R}^{n_{DOF} \times n_{DOF}}$ represent the mass, damping and stiffness of the structure, respectively. $\mathbf{M}_h(\omega)$ and $\mathbf{C}_h(\omega) \in \mathbb{R}^{n_{DOF} \times n_{DOF}}$ are the hydrodynamic frequency-dependent added mass and potential damping, respectively, and $\mathbf{K}_h \in \mathbb{R}^{n_{DOF} \times n_{DOF}}$ is the hydrostatic restoring stiffness.

The (complex) eigenmodes of the system can be found by solving the eigenvalue problem obtained when equating Eq. 1 to zero. This is often the desired approach in frequency-domain studies of floating structures and gives insight into the natural frequencies and damping of the coupled fluid-structure system [20]. In this case, however, a time-domain model of the system is sought. An equivalent time-domain formulation of Eq. 1 is found by applying the inverse Fourier transform, yielding the formulation known as the Cummins equation:

$$(\mathbf{M}_s + \mathbf{M}_{h,\infty})\ddot{\mathbf{u}}(t) + \mathbf{C}_s\dot{\mathbf{u}}(t) + (\mathbf{K}_s + \mathbf{K}_h)\mathbf{u}(t) + \mathbf{p}_{mi}(t) = \mathbf{L}_p\mathbf{p}_w(t) \tag{2}$$

Here, $\mathbf{M}_{h,\infty}$ is defined as $\lim_{\omega\to\infty} \mathbf{M}_h(\omega)$, which in practice converges for frequencies far less than infinity. Due to the frequency dependency of the hydrodynamic mass and damping, the so-called radiation or motion-induced forces $\mathbf{p}_{mi}(t) \in \mathbb{R}^{n_{DOF}}$ appear as a convolution integral:

$$\mathbf{p}_{mi}(t) = \int_0^t \mathbf{h}(t-\tau)\mathbf{u}(\tau)\,\mathrm{d}\tau \tag{3}$$

The convolution memory kernel $\mathbf{h}(t)$ is the inverse Fourier transform of the following transfer function:

$$\mathbf{h}(\omega) = i\omega\mathbf{C}_h(\omega) - \omega^2(\mathbf{M}_h(\omega) - \mathbf{M}_{h,\infty}) \tag{4}$$

It is also possible to consider these motion-induced forces as an external stimulus as felt by the structure [21]. In the presented study it is however desired to only have one source of (unknown) external loading on the pontoons, i.e. the wave excitation forces.

We seek a linear time-invariant [..[2]]system model of Eq. 2[..[3]]. This implies the direct convolution must be avoided, and is carried out in an approximation step as described in the following. We assume that the transfer function

[2] removed: approximation of the system in

[3] removed: so that the convolution can be avoided

$\mathbf{h}(\omega) \in \mathbb{C}^{\mathrm{n_{DOF}} \times \mathrm{n_{DOF}}}$ can be substituted by the following parametric expression, known as Rogers' approximation [22], commonly used in, for example, wind engineering [23, 24]:

$$\hat{\mathbf{h}}(\omega) = \sum_{l=1}^{N_l} \mathbf{a}_l \frac{i\omega}{i\omega + d_l} \tag{5}$$

where the hat symbol indicates an approximated quantity. The order N_l determines the number of terms in the approximation. It can be shown that the expression in Eq. 5 is a partial fraction decomposition of a rational transfer function, and it is a so-called common denominator model since the poles of the transfer function ($-d_l \in \mathbb{R}$) are shared among all the wetted DOFs. Similar approaches have been used to model marine structures, where it is more common to use the polynomial form of rational transfer functions directly [16].

Eq. 5 has the following real and imaginary parts:

$$\mathrm{Re}(\hat{\mathbf{h}}(\omega)) = \sum_{l=1}^{N_l} \mathbf{a}_l \frac{\omega^2}{d_l^2 + \omega^2} \tag{6}$$

$$\mathrm{Im}(\hat{\mathbf{h}}(\omega)) = \sum_{l=1}^{N_l} \mathbf{a}_l \frac{d_l \omega}{d_l^2 + \omega^2} \tag{7}$$

From Eq. 4, it is seen that the mass and damping can be reconstructed in the parametric model by the following expressions:

$$\hat{\mathbf{M}}_\mathrm{h}(\omega) = \frac{\mathrm{Re}(\hat{\mathbf{h}}(\omega))}{-\omega^2} + \mathbf{M}_{\mathrm{h},\infty} = \sum_{l=1}^{N_l} \mathbf{a}_l \frac{-1}{d_l^2 + \omega^2} + \mathbf{M}_{\mathrm{h},\infty} \tag{8}$$

$$\hat{\mathbf{C}}_\mathrm{h}(\omega) = \frac{\mathrm{Im}(\hat{\mathbf{h}}(\omega))}{\omega} = \sum_{l=1}^{N_l} \mathbf{a}_l \frac{d_l}{d_l^2 + \omega^2} \tag{9}$$

In the cases where the hydrodynamic matrices are given at discrete frequencies ($\omega_r > 0$), the coefficients of $\mathbf{a}_l \in \mathbb{R}^{\mathrm{n_{DOF}} \times \mathrm{n_{DOF}}}$ and $d_l > 0$ ($l = 1 \ldots N$) can be found by minimizing the objective function:

$$\sum_{r \in \{\omega\}} \sum_{i,j} W(\omega_r) \Big((\hat{M}_{\mathrm{h},ij}(\omega_r) - M_{\mathrm{h},ij}(\omega_r))^2 + (\hat{C}_{\mathrm{h},ij}(\omega_r) - C_{\mathrm{h},ij}(\omega_r))^2 \Big) \tag{10}$$

where the indices ij select the non-zero matrix elements (i.e.[..[4]] the wetted DOFs). This fit is a non-linear least squares problem, where the objective is to reconstruct the hydrodynamic mass and damping in the parametric model. $W(\omega_r)$ is an optional penalty weight assignment, which can be used to emphasise a frequency range of interest.

Next, a truncation is performed. First, the following eigenvalue problem is solved:

$$[\mathbf{K}_\mathrm{s} + \mathbf{K}_\mathrm{h} - \omega_j^2 (\mathbf{M}_\mathrm{s} + \mathbf{M}_{\mathrm{h},\infty})]\boldsymbol{\phi}_j = \mathbf{0} \qquad (j = 1 \ldots \mathrm{n_m}) \tag{11}$$

[4] removed: ,

We introduce the truncation $\mathbf{u}(t) \approx \mathbf{\Phi}\mathbf{z}(t)$, where $\mathbf{\Phi} \in \mathbb{R}^{n_{DOF} \times n_m}$ contains n_m mass-normalised eigenvectors and $\mathbf{z}(t) \in \mathbb{R}^{n_m}$ is the generalised coordinate vector. [..[5]]Next, the following [..[6]]truncation relations are used:

$$\mathbf{\Phi}^T(\mathbf{M}_s + \mathbf{M}_{h,\infty})\mathbf{\Phi} = \mathbf{I} \tag{12}$$

$$\mathbf{\Phi}^T(\mathbf{K}_s + \mathbf{K}_h)\mathbf{\Phi} = \mathbf{\Omega}^2 \tag{13}$$

$$\mathbf{\Phi}^T\mathbf{C}_s\mathbf{\Phi} = 2\mathbf{\Omega}\mathbf{\Xi} \tag{14}$$

where $\mathbf{\Omega} = \mathrm{diag}(\omega_j) \in \mathbb{R}^{n_m \times n_m}$ and $\mathbf{\Xi} = \mathrm{diag}(\xi_j) \in \mathbb{R}^{n_m \times n_m}$. Note that Eq. 14 [..[7]]is purely an assumption on the proportionality of the damping matrix $\mathbf{C}_s$. Full damping matrices are rarely known explicitly, but the modal damping ratios (ξ_j) of the structure are often approximately known. Furthermore, even though $\mathbf{\Phi}$ does not represent the true vibration modes of the combined structure-fluid system, Eq. 14 is used as a simplified way to introduce the structure-borne damping into the model.

We remark that a classic modal truncation of the system in Eq. 1 is not possible in this case due to the frequency dependency of the system matrices. The truncation we apply still exploits the property [..[8]]that the shapes in $\mathbf{\Phi}$ from the sub-system in Eq. 11 will be similar to the system eigenmodes of Eq. 1. The column vectors of $\mathbf{\Phi}$ therefore serve as a set of shapes that is efficient in the model order reduction of the time-invariant model. However, since $\mathbf{\Phi}$ does not contain the system eigenmodes in the true meaning of the term, we refer to the truncation as a generalised one rather than a classic modal reduction. The truncation results in a generalised equation of motion when Eq. 2 is premultiplied by $\mathbf{\Phi}^T$:

$$\ddot{\mathbf{z}}(t) + 2\mathbf{\Omega}\mathbf{\Xi}\dot{\mathbf{z}}(t) + \mathbf{\Omega}^2\mathbf{z}(t) + \mathbf{\Phi}^T\mathbf{p}_{mi}(t) = \mathbf{\Phi}^T\mathbf{L}_p\mathbf{p}_w(t) \tag{15}$$

The parametric modelling of the (generalised) motion-induced forces in the frequency domain now becomes:

$$\mathbf{\Phi}^T\mathbf{p}_{mi}(\omega) = \mathbf{\Phi}^T\mathbf{h}(\omega)\mathbf{u}(\omega) \approx \mathbf{\Phi}^T\hat{\mathbf{h}}(\omega)\mathbf{\Phi}\mathbf{z}(\omega) = \sum_{l=1}^{N_l} \mathbf{\Phi}^T\mathbf{a}_l\mathbf{\Phi}\frac{i\omega}{i\omega + d_l}\mathbf{z}(\omega) = \sum_{l=1}^{N_l} \mathbf{\Phi}^T\mathbf{a}_l\mathbf{\Phi}\boldsymbol{\mu}_l(\omega) \tag{16}$$

where, in the last step, the following frequency-domain definition of the vector $\boldsymbol{\mu}_l(\omega) \in \mathbb{C}^{n_m}$ is introduced:

$$\boldsymbol{\mu}_l(\omega) = \frac{i\omega}{i\omega + d_l}\mathbf{z}(\omega) \tag{17}$$

Using the inverse Fourier transform, this equation translates to a first-order differential equation in the time domain:

$$\dot{\boldsymbol{\mu}}_l(t) = -d_l\boldsymbol{\mu}_l(t) + \dot{\mathbf{z}}(t) \tag{18}$$

Alternatively, this can be formulated for all the poles ($l = 1 \ldots N_l$):

[5] removed: From the truncation

[6] removed: relations hold

[7] removed: assumes that the damping is proportional, i. e., $\mathbf{\Phi}$ diagonalises $\mathbf{C}_s$ such that only the damping from the structure is given by the modal damping ratios, denoted as

[8] removed: in which

$$\begin{bmatrix} \dot{\boldsymbol{\mu}}_1(t) \\ \vdots \\ \dot{\boldsymbol{\mu}}_{N_l}(t) \end{bmatrix} = \begin{bmatrix} -d_1\mathbf{I} & & \\ & \ddots & \\ & & -d_{N_l}\mathbf{I} \end{bmatrix} \begin{bmatrix} \boldsymbol{\mu}_1(t) \\ \vdots \\ \boldsymbol{\mu}_{N_l}(t) \end{bmatrix} + \begin{bmatrix} \mathbf{I} \\ \vdots \\ \mathbf{I} \end{bmatrix} \dot{\mathbf{z}}(t) \tag{19}$$

or written in compact matrix form:

$$\dot{\mathbf{q}}(t) = \hat{\mathbf{A}}\mathbf{q}(t) + \hat{\mathbf{B}}\dot{\mathbf{z}}(t) \tag{20}$$

where we define the state $\mathbf{q}(t) = [\boldsymbol{\mu}_1(t)^\mathrm{T} \ \dots \ \boldsymbol{\mu}_{N_l}(t)^\mathrm{T}]^\mathrm{T} \in \mathbb{R}^{N_l \mathrm{n_m}}$. The state elements in $\mathbf{q}(t)$ do not have a particular physical meaning; they can be seen as variables assisting in modelling the motion-induced forces. The summation in the time-domain form of Eq. 16 may also be written in matrix form:

$$\boldsymbol{\Phi}^\mathrm{T}\mathbf{p}_\mathrm{mi}(t) = \begin{bmatrix} \boldsymbol{\Phi}^\mathrm{T}\mathbf{a}_1\boldsymbol{\Phi} & \dots & \boldsymbol{\Phi}^\mathrm{T}\mathbf{a}_{N_l}\boldsymbol{\Phi} \end{bmatrix} \begin{bmatrix} \boldsymbol{\mu}_1(t) \\ \vdots \\ \boldsymbol{\mu}_{N_l}(t) \end{bmatrix} = \hat{\mathbf{C}}\mathbf{q}(t) \tag{21}$$

The obtained matrices $\hat{\mathbf{A}} \in \mathbb{R}^{N_l \mathrm{n_m} \times N_l \mathrm{n_m}}$, $\hat{\mathbf{B}} \in \mathbb{R}^{N_l \mathrm{n_m} \times \mathrm{n_m}}$, and $\hat{\mathbf{C}} \in \mathbb{R}^{\mathrm{n_m} \times N_l \mathrm{n_m}}$ are time-invariant, which is desired to replace the convolution in Eq. 3. The coupled system dynamics can finally be described by combining Eq. 15, 20 and 21 in state-space form:

$$\begin{bmatrix} \dot{\mathbf{z}}(t) \\ \ddot{\mathbf{z}}(t) \\ \dot{\mathbf{q}}(t) \end{bmatrix} = \begin{bmatrix} \mathbf{0} & \mathbf{I} & \mathbf{0} \\ -\boldsymbol{\Omega}^2 & -2\boldsymbol{\Omega}\boldsymbol{\Xi} & -\hat{\mathbf{C}} \\ \mathbf{0} & \hat{\mathbf{B}} & \hat{\mathbf{A}} \end{bmatrix} \begin{bmatrix} \mathbf{z}(t) \\ \dot{\mathbf{z}}(t) \\ \mathbf{q}(t) \end{bmatrix} + \begin{bmatrix} \mathbf{0} \\ \mathbf{I} \\ \mathbf{0} \end{bmatrix} \boldsymbol{\Phi}^\mathrm{T}\mathbf{L}_\mathrm{p}\mathbf{p}_\mathrm{w}(t) \tag{22}$$

This can also be written in compact matrix form:

$$\dot{\mathbf{x}}(t) = \mathbf{A}_\mathrm{c}\mathbf{x}(t) + \mathbf{B}_\mathrm{c}\mathbf{p}(t) \tag{23}$$

For reasons which will be explained later, we have defined $\mathbf{p}(t) = \boldsymbol{\Phi}^\mathrm{T}\mathbf{L}_\mathrm{p}\mathbf{p}_\mathrm{w}(t)$ such that generalised forces $\mathbf{p}(t) \in \mathbb{R}^{\mathrm{n_m}}$ are used instead of the wave forces directly. The state vector is now $\mathbf{x}(t) = [\mathbf{z}(t)^\mathrm{T} \quad \dot{\mathbf{z}}(t)^\mathrm{T} \quad \mathbf{q}(t)^\mathrm{T}]^\mathrm{T} \in \mathbb{R}^{\mathrm{n_s}}$ with continuous system matrices $\mathbf{A}_\mathrm{c} \in \mathbb{R}^{\mathrm{n_s} \times \mathrm{n_s}}$ and $\mathbf{B}_\mathrm{c} \in \mathbb{R}^{\mathrm{n_s} \times \mathrm{n_m}}$, where the state order is $\mathrm{n_s} = (2 + N_l)\mathrm{n_m}$. For some applications of the state-space model, it is convenient to limit the state order to reduce the computational burden. Thus, the order N_l must be chosen while keeping in mind both the approximation accuracy and the resulting size of the system model.

Next, measurements of the accelerations and displacements are considered. Using the binary matrices $\mathbf{S}_\mathrm{a}$ and $\mathbf{S}_\mathrm{d} \in \mathbb{R}^{\mathrm{n_y} \times \mathrm{n_{DOF}}}$ to select the measured DOFs, the output vector $\mathbf{y}(t) \in \mathbb{R}^{\mathrm{n_y}}$ becomes:

$$\begin{aligned} \mathbf{y}(t) &= \mathbf{S}_\mathrm{a}\ddot{\mathbf{u}}(t) + \mathbf{S}_\mathrm{d}\mathbf{u}(t) \approx \mathbf{S}_\mathrm{a}\boldsymbol{\Phi}\ddot{\mathbf{z}}(t) + \mathbf{S}_\mathrm{d}\boldsymbol{\Phi}\mathbf{z}(t) \\ &= \begin{bmatrix} \mathbf{S}_\mathrm{d}\boldsymbol{\Phi} - \mathbf{S}_\mathrm{a}\boldsymbol{\Phi}\boldsymbol{\Omega}^2 & -\mathbf{S}_\mathrm{a}\boldsymbol{\Phi}2\boldsymbol{\Omega}\boldsymbol{\Xi} & -\mathbf{S}_\mathrm{a}\boldsymbol{\Phi}\hat{\mathbf{C}} \end{bmatrix} \begin{bmatrix} \mathbf{z}(t) \\ \dot{\mathbf{z}}(t) \\ \mathbf{q}(t) \end{bmatrix} + \begin{bmatrix} \mathbf{S}_\mathrm{a}\boldsymbol{\Phi} \end{bmatrix} \boldsymbol{\Phi}^\mathrm{T}\mathbf{L}_\mathrm{p}\mathbf{p}_\mathrm{w}(t) \\ &= \mathbf{G}_\mathrm{c}\mathbf{x}(t) + \mathbf{J}_\mathrm{c}\mathbf{p}(t) \end{aligned} \tag{24}$$

where $\mathbf{G}_c \in \mathbb{R}^{n_y \times n_s}$ and $\mathbf{J}_c \in \mathbb{R}^{n_y \times n_m}$. [..[9]]By imposing a zero-order-hold assumption on the input, we now discretise the state-space formulation by a time step Δt such that $t_k = k\Delta t$ ($k = 0, 1, \ldots, N_t - 1$):

$$\mathbf{x}_{k+1} = \mathbf{A}\mathbf{x}_k + \mathbf{B}\mathbf{p}_k \tag{25}$$

$$\mathbf{y}_k = \mathbf{G}\mathbf{x}_k + \mathbf{J}\mathbf{p}_k \tag{26}$$

where $\mathbf{x}_k = \mathbf{x}(t_k)$, $\mathbf{p}_k = \mathbf{p}(t_k)$ and $\mathbf{y}_k = \mathbf{y}(t_k)$. The discrete time system matrices are given as follows:

$$\mathbf{A} = \exp\left(\mathbf{A}_c \Delta t\right), \quad \mathbf{B} = (\mathbf{A} - \mathbf{I})\mathbf{A}_c^{-1}\mathbf{B}_c, \quad \mathbf{G} = \mathbf{G}_c, \quad \mathbf{J} = \mathbf{J}_c \tag{27}$$

It can be noted that when the frequency-dependent mass and damping are neglected, the matrices $\hat{\mathbf{A}}$, $\hat{\mathbf{B}}$ and $\hat{\mathbf{C}}$ vanish, and the resulting state-space model becomes an ordinary model of a linear system with n_m modes. For floating bridges, however, the mass and damping from the fluid plays a large role in the dynamics of the structure and cannot be neglected.

The established state-space system is the model basis used in the identification of the input forces via inverse methods, which is further elaborated in Section 4.1.

3. The Bergsøysund Bridge

3.1. Description of the bridge and instrumentation

The Bergsøysund Bridge, shown in Fig. 2, is located on the west coast of Norway. The bridge consists of a steel truss superstructure supported by seven concrete pontoons. The structure is anchored only at the end supports and has a floating span of 840 m.

The monitoring system at the site, which is described in detail in [25], can be summarised as follows: two triaxial accelerometers are installed at each of the seven pontoons, five sonic anemometers are mounted on lampposts and six wave radars are mounted on the steel superstructure. Note that the wave radars have been moved from their original locations given in [25] and are now clustered together, as shown in Fig. 1. The current configuration of these sensors makes it feasible to identify the directional wave spectrum, which is discussed further in Section 4.2.

3.2. System model

The modelling part of the structure utilises two different software programs. The first is the wave-structure interaction software HydroD WADAM, which is based on first-order potential theory. Panel models of the pontoons are created in this program (Fig. 3), where a single pontoon is assumed to behave as a rigid object, meaning its local mass, damping and stiffness properties can be described by 6×6 matrices, representing its six local DOFs. From HydroD, the matrices $\mathbf{K}_h$, $\mathbf{C}_h(\omega)$ and $\mathbf{M}_h(\omega)$ are obtained for frequencies up to 15 rad/s or 2.4 Hz. The second software used is the FE program ABAQUS, in which the steel superstructure is modelled; see Fig. 3. In the FE model, the pontoons are replaced with dummy rigid body objects, which are assigned nodal stiffness $\mathbf{K}_h$ and mass $\mathbf{M}_{h,\infty}$, meaning that the natural frequencies and generalised modes obtained from the ABAQUS model equal those given in Eq. 11.

[9] removed: We

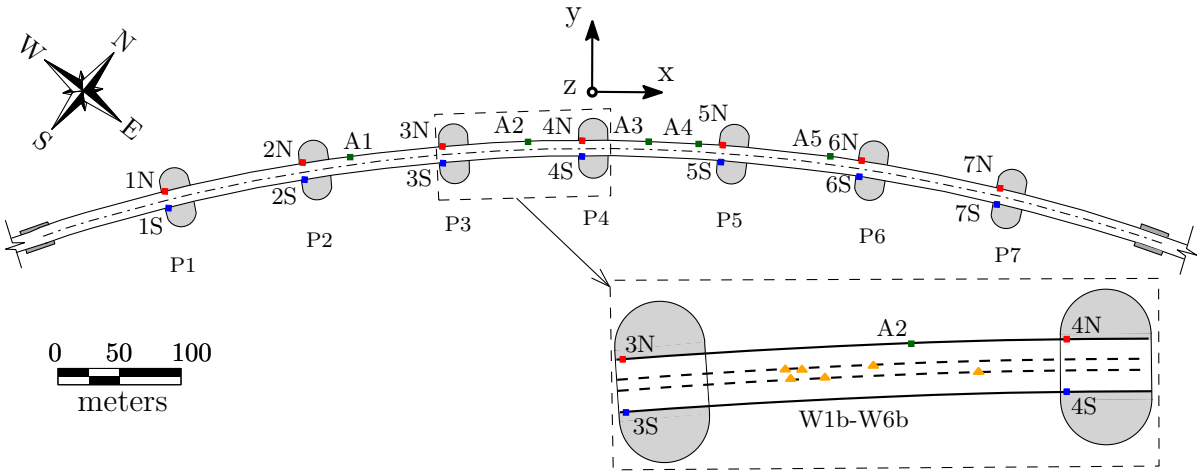

Figure 1: Instrumentation of the bridge: accelerometers 1S-7S/1N-7N (blue/red squares), anemometers (green squares) and wave radars (orange triangles).

Figure 2: The Bergsøysund bridge, as seen from the south.

A non-linear least squares solver is used to fit the coefficients $\mathbf{a}_l$ and d_l by minimizing Eq. 10. The [..[10]]residual penalty weights $W(\omega)$ are chosen as the first singular value of a power spectral density (PSD) matrix of measured acceleration data from the bridge. This penalty emphasizes a low frequency range (0 – 6 rad/s), but is found to not have a large significance here. As shown in Fig. 4, the hydrodynamic curves are quite smooth, which tends to give a good fit along the whole frequency axis. The hydrodynamic mass of a single pontoon has the following local structure:

$$\begin{bmatrix} M_{\mathrm{h},11}(\omega) & 0 & 0 & 0 & M_{\mathrm{h},15}(\omega) & 0 \\ 0 & M_{\mathrm{h},22}(\omega) & 0 & M_{\mathrm{h},24}(\omega) & 0 & 0 \\ 0 & 0 & M_{\mathrm{h},33}(\omega) & 0 & 0 & 0 \\ 0 & M_{\mathrm{h},24}(\omega) & 0 & M_{\mathrm{h},44}(\omega) & 0 & 0 \\ M_{\mathrm{h},15}(\omega) & 0 & 0 & 0 & M_{\mathrm{h},55}(\omega) & 0 \\ 0 & 0 & 0 & 0 & 0 & M_{\mathrm{h},66}(\omega) \end{bmatrix} \tag{28}$$

where indices 1-6 represent sway, surge, heave, roll, pitch and yaw, respectively (cf. Fig. 3). Here, only 8 elements are unique and non-zero due to the symmetry planes in the pontoon layout and the matrix symmetry. The local hydrodynamic damping matrix is structured similarly. In the parametric modelling of these matrices (Eq. 8 and 9), it is found that the ap-

[10] removed: hydrodynamic

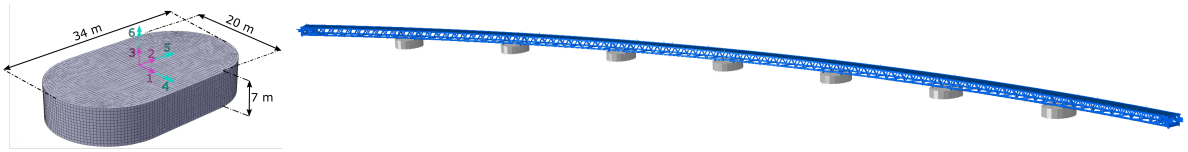

Figure 3: Left: HydroD model of a pontoon; right: ABAQUS model of the bridge.

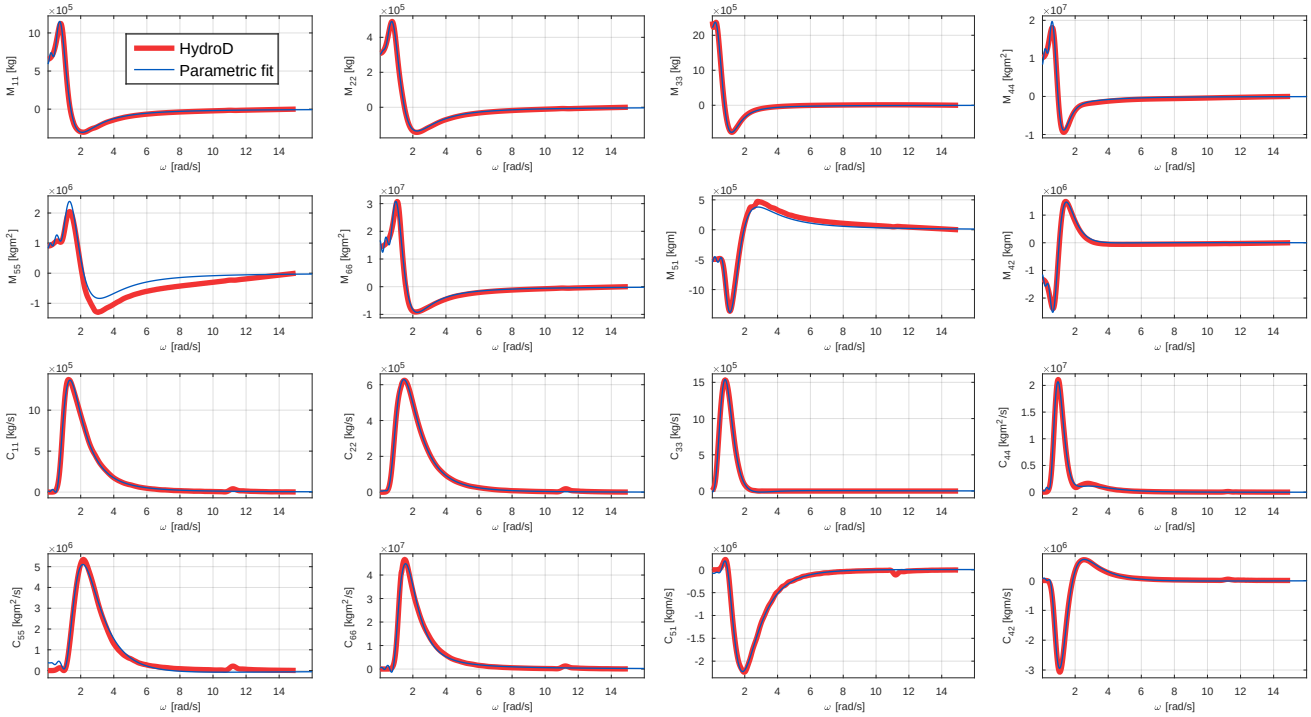

Figure 4: Added mass ($M_{\mathrm{h},ij}(\omega) - M_{\mathrm{h},ij,\infty}$) and potential damping $C_{\mathrm{h},ij}(\omega)$ for the middle pontoon. M_{11}, M_{22}, M_{33}, M_{44}, M_{55} and M_{66} denote diagonal elements of the local 6×6 sub-matrix. M_{51} (=M_{15}) and M_{42} (=M_{24}) are the off-diagonal elements. The same convention holds for the elements of the damping matrix.

proximation order $N_l = 8$ yields a good trade-off in terms of accuracy vs. system size when the coefficients $\mathbf{a}_l$ and d_l are fitted by minimising Eq. 10. In Fig. 4, the hydrodynamic mass and damping for the middle pontoon are shown, as well as both the non-parametric data from HydroD and the reconstructed mass and damping from the parametric fit. Small discrepancies are visible; M_{55} has the largest relative deviation. While not shown here, a similar goodness of fit is obtained for the other pontoons.

As the structure is primarily excited by waves, generalised modes from Eq. 11 with natural frequencies up to 5 rad/s (0.8 Hz) are included in the model ($\mathrm{n_m} = 18$). These modes are shown in Fig. 5. Due to the curved shape of the bridge, many of the generalised modes are a combination of bending and torsion. A structural damping ratio of $\xi_j = 0.5\%$ is assumed for all modes. As already mentioned, these damping ratios represent the approximate level of damping from the structure only. Operational modal analysis indicate that damping ratios of $0.3 - 1\%$ is reasonable for this bridge [26], when only the structural damping is considered. Thus, 0.5% is deemed a qualified guess that is reasonable for a welded steel structure. Furthermore, changing the assigned damping does not significantly alter the results.

The resulting state order for the employed state-space model becomes $\mathrm{n_s} = 180$.

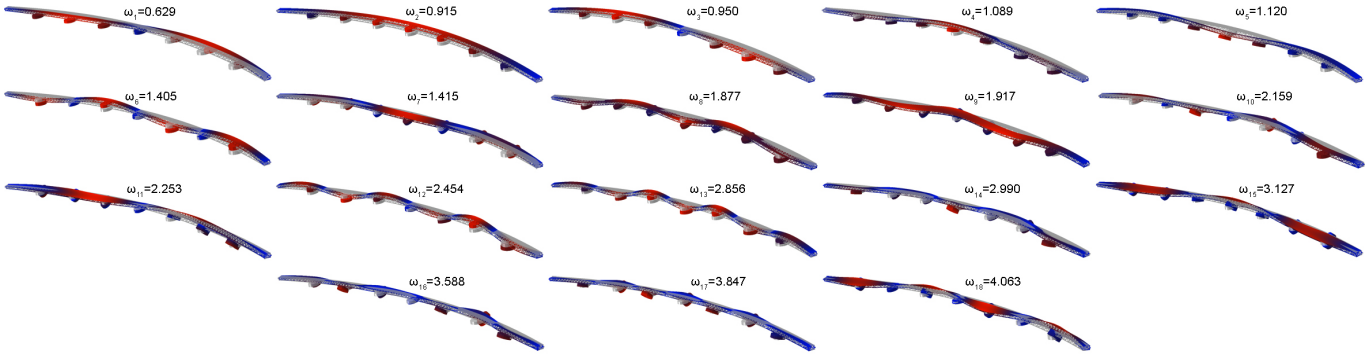

Figure 5: Generalised modes of the model, with the corresponding frequency ω_j given in rad/s.

4. Methods for identification of wave forces

4.1. Estimation by inverse identification algorithms

The techniques used in this study for the inverse identification of forces can be classified as stochastic-deterministic methods. This implies the addition of zero-mean white noise vectors to Eq. 25 and 26:

$$\mathbf{x}_{k+1} = \mathbf{A}\mathbf{x}_k + \mathbf{B}\mathbf{p}_k + \mathbf{w}_k \tag{29}$$

$$\mathbf{y}_k = \mathbf{G}\mathbf{x}_k + \mathbf{J}\mathbf{p}_k + \mathbf{v}_k \tag{30}$$

The following covariance relations are used to describe the process noise $\mathbf{w}_k \in \mathbb{R}^{n_s}$ and measurement noise $\mathbf{v}_k \in \mathbb{R}^{n_y}$:

$$\mathbb{E}[\mathbf{w}_k\mathbf{w}_l^T] = \mathbf{Q}\delta_{kl}, \quad \mathbb{E}[\mathbf{v}_k\mathbf{v}_l^T] = \mathbf{R}\delta_{kl}, \quad \mathbb{E}[\mathbf{w}_k\mathbf{v}_l^T] = \mathbf{S}\delta_{kl} \tag{31}$$

In this study, we apply a newly developed Kalman-type smoothing algorithm for state and input estimation [9]. This is an extension of the filter in [8], except that a time delay of L time steps is introduced in the estimation. The time-delayed smoother has some advantages compared to a non-delay filter: it can reduce the error uncertainty of the state and input estimates due to the extra information provided by the measurement data in the L time lags, particularly for cases [..[11]]with non-collocated forces. In this context, collocation refers to a configuration where the locations of the vibration sensors coincide with the forces[..[12]], which leads to a strong influence on the output data from the input forces. The time delay smoothing comes at the cost of increased computational time. From this algorithm, state estimates ($\hat{\mathbf{x}}_k$) and input estimates ($\hat{\mathbf{p}}_k$) are available. These estimates can either be utilised directly or be used to extrapolate the response to unmeasured locations.

Since the focus of this paper is input estimation, it is essential to have an initial overview of the types of forces present. The bridge under consideration has three sources of excitation. The first and most important are the wave actions on the pontoons. Second, there are wind actions on the superstructure. Finally, traffic can cause some vibrations, although the traffic density on the Bergsøysund bridge is usually low.

In previous numerical simulations of force identification, it was shown that three of the six wave force components on each pontoon can be neglected in input estimation [27], as they contribute little to the output. However, this assumes a head sea,

[11] removed: where the measurements are not collocated

[12] removed: . This

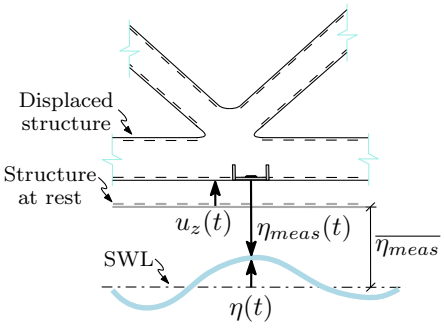

Figure 6: The wave radar setup.

i.e., waves mainly approaching perpendicular to the bridge, which is not always the case in reality. In the context of identifying wave forces, the wind can be seen as an additional stochastic excitation. Previous studies of the bridge show that it is possible to neglect the wind forces and still obtain an adequate estimation of the full-field response using inverse methods [21]. When input estimation is the main goal, however, the resulting input estimates are more sensitive to any unmodelled forces, thus contradicting the system description and therefore manifesting as errors. Even though the system description in Eq. 29-30 includes noise terms, it is not always possible to filter out errors from additional excitation sources, either because they are too large, non-white, or in unknown locations.

All in all, we conclude that in the current case study, there are too many wave forces and additional unknown sources of excitation present. For this reason, we are compelled to identify the total generalised forces on the structure rather than the individual wave force components. The generalised forces $\mathbf{p}_k$ in Eq. 29-30 encompass, by definition, any type of excitation on the structure; thus, the wind and traffic loads are not required to be filtered out by the algorithms. It is expected that these generalised forces will still be dominated by the wave force content for most medium- or high-level sea states.

For input estimation to be possible, the set of theoretical identifiability conditions given in [28] must be fulfilled. It is verified that the employed state-space model fulfils the requirements for invertibility and observability. For the structure under consideration, this means that the inputs can be estimated instantaneously ($L = 0$) or with a time delay ($L > 0$) and that all the states can be observed, i.e., both the generalised coordinates $\mathbf{z}(t)$ and the auxiliary variables $\mathbf{q}(t)$.

4.2. Frequency-domain assessment of wave force spectral densities using wave radar data

In the previous section, the unknown forces considered had no parametric model behind them. In this section, we look at the wave forces from a parametric model of the sea state. It is necessary to assume that the sea surface elevation $\eta(x, y, t)$ is a zero-mean stationary stochastic process that is spatially homogeneous. This process can be characterised by the directional wave spectral density $S_{\eta\eta}(\omega, \theta)$, where θ represents the wave direction. The unidirectional wave spectrum $S_{\eta\eta}(\omega)$ can be obtained by integration over the directions:

$$S_{\eta\eta}(\omega) = \int_0^{2\pi} S_{\eta\eta}(\omega, \theta)\, \mathrm{d}\theta \tag{32}$$

The significant wave height (SWH) is defined as four times the standard deviation of $\eta(t)$:

$$\mathrm{SWH} = 4\Big(\int_{-\infty}^{\infty} S_{\eta\eta}(\omega)\, \mathrm{d}\omega \Big)^{1/2} \tag{33}$$

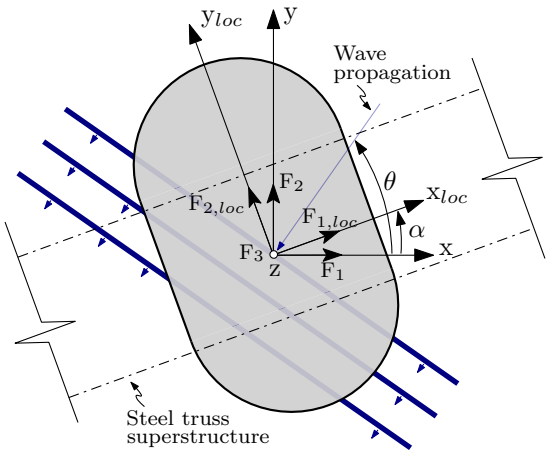

Figure 7: Local and global coordinate axes for a pontoon. The angle α varies from 0° for the middle pontoon to ±14° for the outermost two.

The marginal spectrum for only the directions is found by integration over the frequencies:

$$S_{\eta\eta}(\theta) = \int_{-\infty}^{\infty} S_{\eta\eta}(\omega, \theta)\, \mathrm{d}\omega \tag{34}$$

The approach now considered makes use of the available wave radar data and the transfer functions for wave excitation from the HydroD pontoon model to reconstruct the wave forces in the frequency domain. $S_{\eta\eta}(\omega, \theta)$ can be estimated using data from a distributed array of wave radars. Numerical simulations have shown that it is feasible to reconstruct the wave field at the Bergsøysund bridge with the current positions of the wave radars [29]. In this study, $S_{\eta\eta}(\omega, \theta)$ is estimated by the extended maximum entropy principle (EMEP), implemented in the DIWASP Toolbox for MATLAB [30]. The directional spectrum can, in this method, be interpreted as a probabilistic distribution of the wave energy over the directions; for details, see [31].

The installed wave radars measure the distance from the sensor to the water surface. For this reason, these measurements refer to a dynamic frame of reference since the structure, and therefore also the sensor, is moving. According to Fig. 6, the true sea surface elevation $\eta(t)$ is therefore obtained by adjusting the individual measurement $\eta_{meas}(t)$ as follows:

$$\eta(t) = \overline{\eta_{meas}} - (\eta_{meas}(t) - u_z(t)) \tag{35}$$

where $\overline{\eta_{meas}}$ denotes the mean measured value and $u_z(t)$ is the vertical structural displacement at the location of the radar. The latter quantity is not measured directly but can be estimated from an output equation similar to Eq. 24, letting $\mathbf{S}_\mathrm{a} = \mathbf{0}$ and selecting the vertical displacement at the individual wave radar by the matrix $\mathbf{S}'_\mathrm{d} \in \mathbb{R}^{1\times \mathrm{n_{DOF}}}$:

$$\hat{u}_z(t_k) = \mathbf{S}'_\mathrm{d}\hat{\mathbf{u}}(t_k) = \begin{bmatrix}\mathbf{S}'_\mathrm{d}\boldsymbol{\Phi} & \mathbf{0} & \mathbf{0}\end{bmatrix}\hat{\mathbf{x}}_k \tag{36}$$

Eq. 36 assumes that a state estimate $\hat{\mathbf{x}}_k$ is available, for example, from the algorithms discussed in Section 4.1. For the Bergsøysund bridge, the magnitude of $u_z(t)$ typically amounts to 1-5% of $\eta(t)$. Since this fraction is small, it is, for the sake of simplicity, chosen to neglect $u_z(t)$ to avoid the wave elevation measurements depending on the state estimation.

Provided that $S_{\eta\eta}(\omega, \theta)$ is known, the cross-spectral density of the two first-order wave forces $p^{(m)}_{\mathrm{w},i}$ and $p^{(n)}_{\mathrm{w},j}$ can be calculated by the following integral [32]:

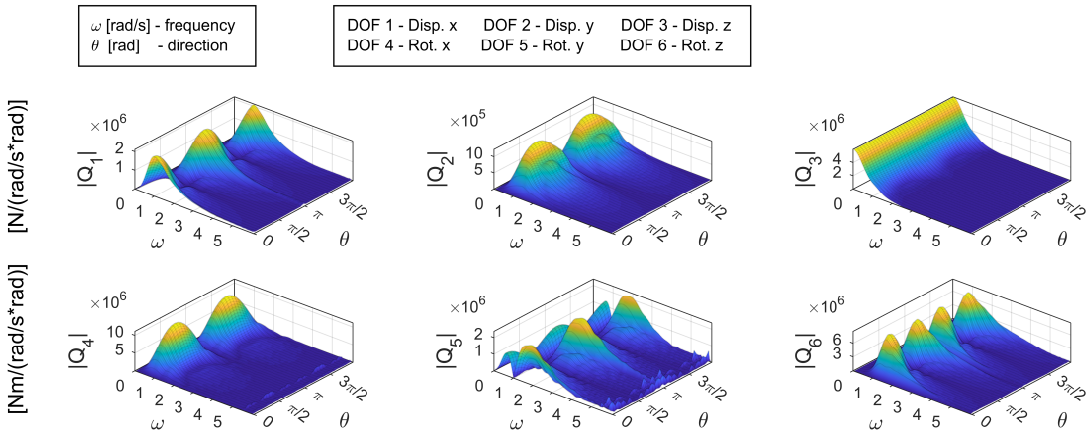

Figure 8: The absolute value of the transfer functions $Q_i(\omega, \theta)$ $(i = 1 \dots 6)$ for the middle pontoon.

$$S_{p_{\mathrm{w},i}^{(m)} p_{\mathrm{w},j}^{(n)}}(\omega) = \int_0^{2\pi} S_{\eta\eta}(\omega, \theta)\, Q_i^{(m)}(\omega, \theta - \alpha_m)\, (Q_j^{(n)}(\omega, \theta - \alpha_n))^*\, \exp\left(- i\kappa(\omega)(\Delta x \cos(\theta) + \Delta y \sin(\theta)\right) \mathrm{d}\theta \tag{37}$$

where the asterisk denotes the complex conjugate and $m, n = \{1 \dots 7\}$ is an index numbering of the pontoons. The sub-indices $i, j = \{1 \dots 6\}$ denote the DOFs of a pontoon, where 1-3 are displacements (or translation forces) and 4-6 are rotations (or moments); see Fig. 3. $\Delta x = x_m - x_n$ and $\Delta y = y_m - y_n$ are the spatial separations between pontoon m and n such that $\Delta x = \Delta y = 0$ when $m = n$. The wave number $\kappa(\omega)$ is given by the dispersion relation, which simplifies to $\kappa(\omega) = \omega^2/g$ for deep water waves ($g = 9.81$ m/s^2). $Q_i^{(m)}(\omega, \theta)$ is the directional transfer function relating wave elevation to wave force for pontoon m; it depends on the incoming wave direction θ. This transfer function is also obtained from the HydroD WADAM pontoon models but in the local xy-coordinate system, as an individual pontoon has a local rotation α with respect to the global coordinate system; see Fig. 7. A transformation into global xy-coordinates is therefore necessary:

$$\begin{bmatrix} Q_1^{(m)} \\ Q_2^{(m)} \\ Q_3^{(m)} \\ Q_4^{(m)} \\ Q_5^{(m)} \\ Q_6^{(m)} \end{bmatrix} = \begin{bmatrix} \cos(\alpha_m) & -\sin(\alpha_m) & 0 & 0 & 0 & 0 \\ \sin(\alpha_m) & \cos(\alpha_m) & 0 & 0 & 0 & 0 \\ 0 & 0 & 1 & 0 & 0 & 0 \\ 0 & 0 & 0 & \cos(\alpha_m) & -\sin(\alpha_m) & 0 \\ 0 & 0 & 0 & \sin(\alpha_m) & \cos(\alpha_m) & 0 \\ 0 & 0 & 0 & 0 & 0 & 1 \end{bmatrix} \begin{bmatrix} Q_{1,loc}^{(m)} \\ Q_{2,loc}^{(m)} \\ Q_{3,loc}^{(m)} \\ Q_{4,loc}^{(m)} \\ Q_{5,loc}^{(m)} \\ Q_{6,loc}^{(m)} \end{bmatrix} \tag{38}$$

The rotation also causes a directional shift in the integrand in Eq. 37. The six directional transfer functions for the middle pontoon are shown in Fig. 8. The pontoons have small variations in their geometry, but their transfer functions are quite similar to the ones shown.

The [..[13]]PSD matrix $\mathbf{S}_{\mathrm{p_w p_w}}(\omega) \in \mathbb{C}^{\mathrm{n_p} \times \mathrm{n_p}}$ containing all the wave forces ($\mathrm{n_p} = 42$) is populated with the elements $S_{p_{\mathrm{w},i}^{(m)} p_{\mathrm{w},j}^{(n)}}(\omega)$ from Eq. 37. For most sea states encountered at the site, the wave forces on two different pontoons are almost uncorrelated due to the large pontoon interdistance; hence, $S_{p_{\mathrm{w},i}^{(m)} p_{\mathrm{w},j}^{(n)}}(\omega) \approx 0$ when $m \neq n$. Since generalised forces are identified using the inverse

[13] removed: power spectral density (PSD)

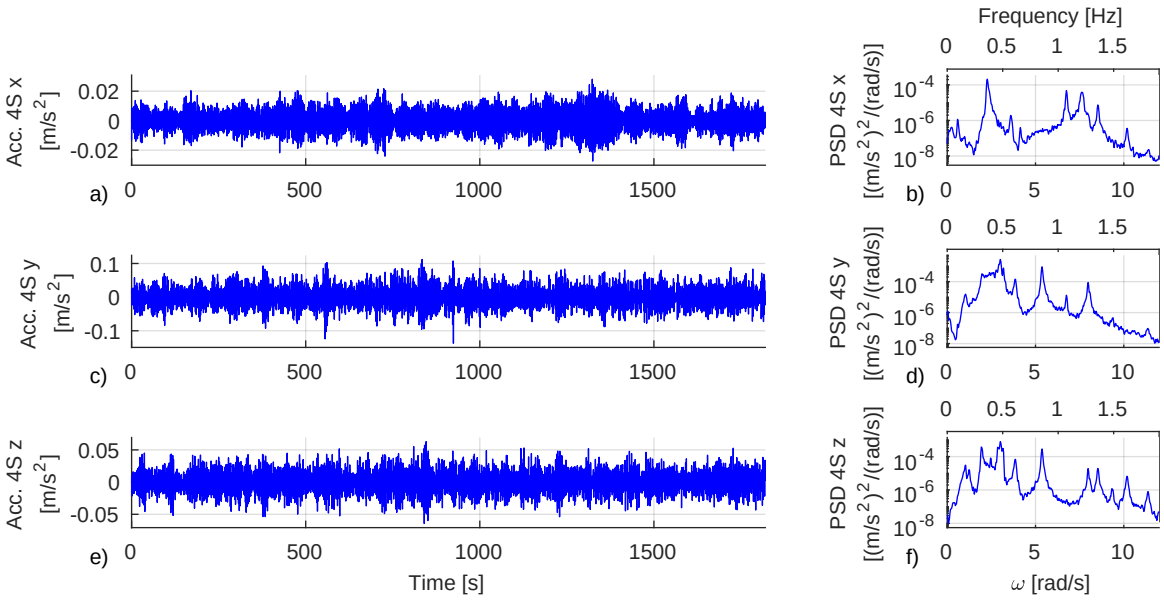

Figure 9: Sample acceleration data from the accelerometer 4S on the middle pontoon.

methods from Section 4.1, $\mathbf{S}_{\mathrm{p_w p_w}}(\omega)$ is transformed into the following generalised form $\mathbf{S}_{\mathrm{pp}}(\omega) \in \mathbb{C}^{\mathrm{n_m} \times \mathrm{n_m}}$ to obtain a common basis of comparison:

$$\mathbf{S}_{\mathrm{pp}}(\omega) = \mathbf{\Phi}^{\mathrm{T}} \mathbf{L}_{\mathrm{p}} \mathbf{S}_{\mathrm{p_w p_w}}(\omega) (\mathbf{\Phi}^{\mathrm{T}} \mathbf{L}_{\mathrm{p}})^{\mathrm{T}} \tag{39}$$

5. Results of wave force identification from measurement data

5.1. Initial assessment and pre-processing of data acquired

The data acquired from the monitoring system is stored in recordings that are 30 minutes long. The acceleration data and wave data are originally sampled at 200 Hz and 50 Hz, respectively, but are resampled to a common rate of 10 Hz for the analysis here. In this study, only recordings with an SWH greater than 0.4 m are considered, as the wave field inhomogeneity is highly reduced as the SWH increases [25]. Note that the homogeneity assumption is required only for the wave field reconstruction (Section 4.2) and not for the inverse methods (Section 4.1).

A recording from 2017-10-02 02:06 is used to illustrate the typical characteristics of the observed data. Fig. 9 shows sample acceleration time series from the south-side accelerometer on the middle pontoon. The response is largest around [..[14]]2 – 3 rad/s (0.3 – 0.5 Hz), which is the range in which the wave energy is concentrated. Fig. 10 shows the recorded wave elevation for three of the wave radars. The SWH is 0.47 m, and the wave elevation appears to be fairly stationary throughout the period. No significant peaks are visible in the wave PSDs (Fig. 10b, d and f); thus, the influence of the structural response on the wave elevation measurements seems negligible, as previously assumed. The wave data are further studied in Fig. 11. Here, a PSD estimate by Welch's method is shown for the individual wave radar W1b-W6b in addition to the estimate from the EMEP

[14] removed: 2-3

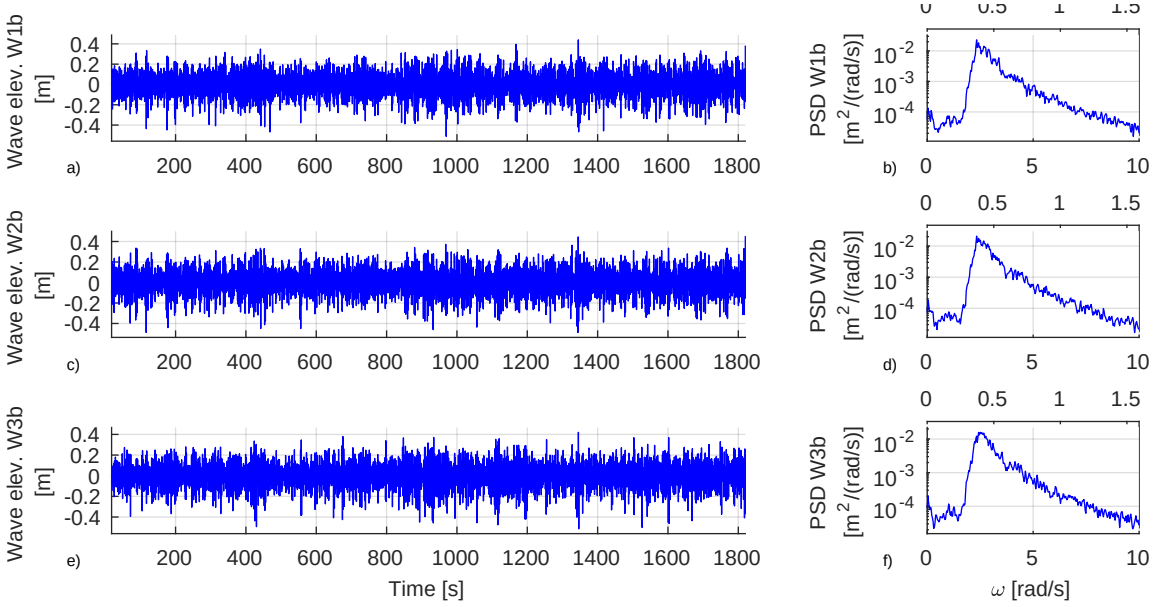

Figure 10: Sample wave elevation data from the three wave radars W1b,W2b and W3b.

estimation (Eq. 34). It appears that the wave field is fairly homogeneous in the middle of the strait, where the wave radars are located.

The acceleration data is low-pass filtered with a cut-off frequency of 4.5 rad/s (0.7 Hz) before it is passed to the force identification algorithm. [..[15]]In practice, static-sensitive [..[16]]output data is necessary in these algorithms, [..[17]]since a divergence is met for a continuous online application with acceleration output only. Here, no static-sensitive data are measured directly, displacement data are [..[18]]in this case [..[19]]generated by numerical integration of the acceleration output data. This is has the convenience of a steady-state convergence of the gain matrices, which reduces the total computational time.

The covariance matrices $\mathbf{Q} = 10^{-2} \times \mathbf{I}$ and $\mathbf{S} = \mathbf{0}$ are used as tuning matrices for the system noise. $\mathbf{R}$ is populated diagonally with 10^{-3} and 10^{-6}, respectively, for the displacement and acceleration outputs to place more emphasis on the accelerations, as this is the quantity that is directly measured. It is known that in practice the white noise assumption is violated. Furthermore, the true "noise" in the system is not really known. Due to the lack of available information, the covariance matrices are assigned constant values on the diagonal, which is a common simplification [2, 4, 7]. The assigned magnitude is approximately a fraction of the variance of the output data and the (unknown) states. In this case, the first-order sensitivity of the results with respect to these covariance matrices is not very significant.

A delay of $L = 10$ time steps in the smoothing is used, leading to a 25-50% reduction in the force error variance compared to an instantaneous inversion ($L = 0$).

[15] removed: It is convenient to also have
[16] removed: data
[17] removed: as this leads to a steady-state convergence of the gain matrices, which reduces the total computational time. Since
[18] removed: ,
[19] removed: ,

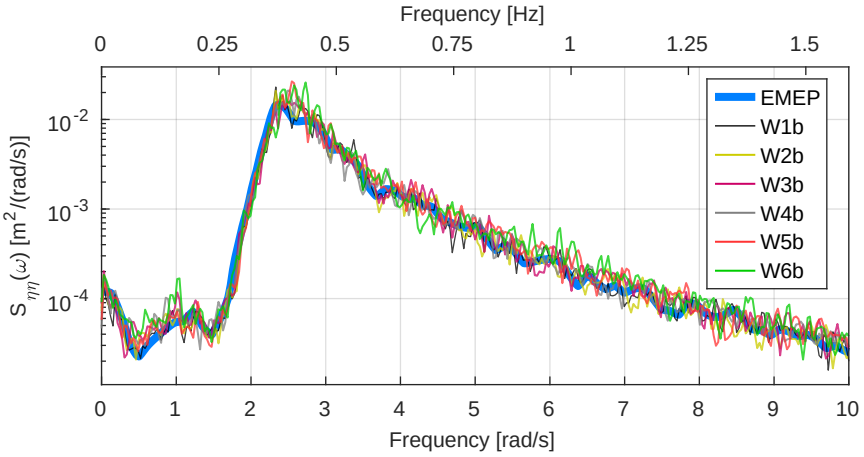

Figure 11: Sample wave spectrum from all six wave radars and the EMEP estimate.

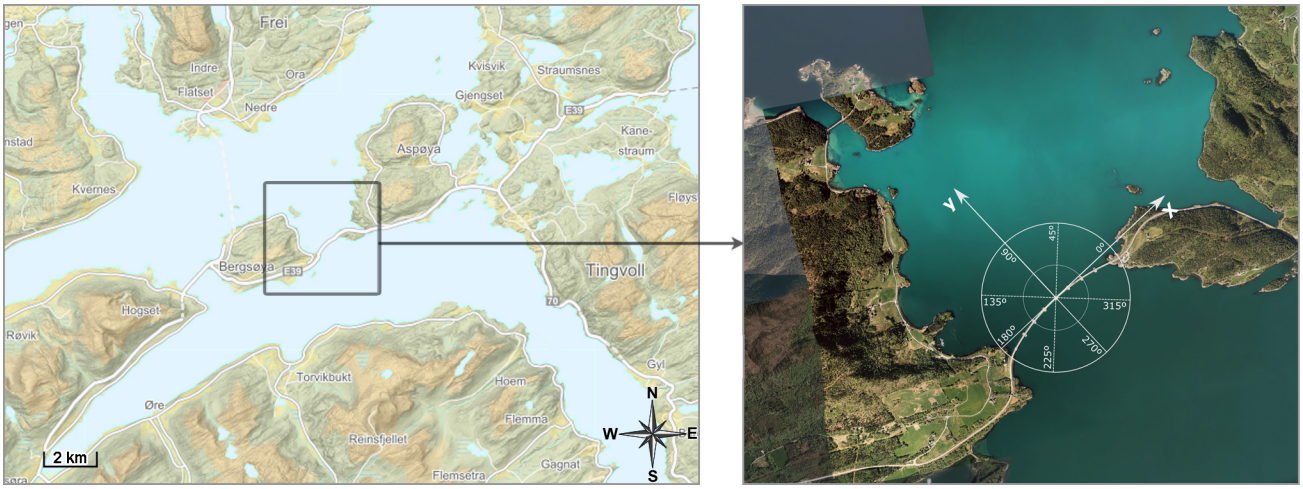

Figure 12: Overview of the coastal geography around the bridge (Photo: Kartverket). The compass shows the definition of the direction θ.

5.2. *Identification of forces*

Four recordings with durations of 30 minutes each are chosen for the estimation of the wave forces. Although more recordings are available, the identification methodology is still young and requires close scrutiny in the evaluation of the results; automatised processing of a larger amount of data is deemed an objective for future work.

The ambient conditions for the four recordings are depicted in Fig. 13, 15, 17 and 19, in the form of a directional wave spectrum estimated from the wave data, as well as the measured wind direction. In all four recordings, the dominant direction of the waves coincides well with the wind direction, which here is reported as the spatial average of all five anemometers. The local coastal geography around the bridge is shown in Fig. 12. In recordings 1, 3 and 4, the waves approach from the fjords to the south, while in recording 2, the northeast fjord at $\theta = 50°$ is the source. The main statistical characteristics of the waves and wind in the four recordings are summarised in Tab. 1. The observed peak periods vary from 2.22 to 3.39 s; higher SWHs tend to yield longer peak periods.

Using the wave data, the PSD matrix of the wave forces is constructed using Eq. 37 and 39, as shown in Fig. 14, 16, 18 and 20. The figures also show the forces identified by the smoothing algorithm driven by acceleration data, where the PSDs

Recording	Date and time	SWH [m]	Peak period [s]	Dominant wave direction [deg]	Mean wind velocity [deg]	Mean wind direction [deg]
1	2017-10-02 02:06	0.47	2.67	250	13.1	252
2	2017-10-29 08:33	0.77	3.39	50	13.1	65
3	2018-01-15 22:57	0.43	3.03	300	12.7	285
4	2018-01-24 14:13	0.44	2.22	296	12.3	281

Table 1: Overview of the wave and wind conditions in the four recordings.

of the time series are calculated by Welch's method. An important point to emphasise is that a direct comparison of the two force estimates can be problematic, as they stem from two separate approaches based on different assumptions. Caution should be taken in the result evaluation since it is not a given that either one represents a "correct" solution. Sources of uncertainties in the two approaches are further discussed in the next section. The results still indicate that the force estimates appear to be reasonable within the range 2 – 4 rad/s (0.3 – 0.6 Hz), in which it is expected that the first-order wave forces are concentrated.

It is apparent that low-frequent content occurs within the range 0 – 1 rad/s (0 – 0.15 Hz) in both force estimates, a characteristic which is not typical of wind-driven sea states. However, this can be the result of two different reasons for the two approaches. For the inverse methods, it is likely due to a combination of model errors and inaccuracies in the accelerometer data close to the zero frequency, causing the force estimates to inflate to unrealistic values. In the forces estimated from the wave data, the zero tail increase as $\omega \to 0$ primarily originates from the transfer function $Q_3(\omega, \theta)$, which has its maximum at the zero frequency (cf. Fig. 8). The generalised modes with significant vertical motion at the pontoons, for example, 2, 3, 4, 12 and 13, are therefore prone to this zero-tail content. This also depends on the value of $S_{\eta\eta}(\omega)$, which, for most of our experimental data, does not decay towards zero but has a plateau within the range 0 – 1 rad/s (0 – 0.15 Hz)similar to the one in Fig. 11. It is not certain that this plateau represents the true physics of the wave elevation; it could be an artefact of measurement inaccuracies or low-frequency vertical movement of the structure due to wind (cf. Eq. 35). In comparison, parametric wave spectra such as JONSWAP decay as $1/\omega^5$ close to the zero frequency and thus do not include any [..[20]]low-frequent waves, as it is common to have separate spectra for wind sea and swell sea. Second-order-difference wave forces can, in reality, also occur at lower frequencies. These are, however, usually magnitudes smaller than the first-order forces.

Overall, recording 2 (Fig. 15 and 16) has the best agreement. When evaluating the observed discrepancy in the force PSDs, it is difficult to point out a strong trend between the recordings. This could be explained by the fact that the four recordings have different load characteristics in terms of wave frequencies and directions. Small changes in the wave directions can cause a large change in the occurring loads, as the transfer functions $Q_i^{(m)}(\omega, \theta)$ (Fig. 8) are highly dependent on the direction. Similarly, a small frequency shift in the wave spectrum can lead to a large change in the generalised load, especially since the generalised modes are closely clustered together.

[20]removed: low-frequency

5.3. Sources of uncertainties

It is clear that for real-life case studies of force identification, uncertainties from various sources will play a significant role. The sources that are deemed most important are discussed here.

There are two main sources of uncertainties in the state-space model that need to be considered. The first are the errors in the dynamic model itself, i.e., the generalised modal properties or the hydrodynamic model, which manifest as an error both in the process equation (Eq. 29) and the output equation (Eq. 30). The second is the measurement uncertainty of the sensors, which affects only the output equation. The signal-to-noise ratio is very [..[21]]high for the acceleration sensors; thus, we expect that the model errors dominate the uncertainties brought into the analysis. For the generated displacement data, small errors can also arise from the numerical integration.

Even though the Kalman-type algorithms provide uncertainty covariance for the estimated states and forces, it is only correct if the noise description in Eq. 31 holds true, i.e., if the noise is truly white and the true noise covariance matrices are prescribed [8]. Since we know that these assumptions are violated in the case presented, it is difficult to directly quantify the uncertainties of the input estimates. Even with the current models of floating bridges, there are aspects of the observed response that are not fully understood or well predicted; thus, the numerical models of these structures do have uncertainties that are seldom negligible.

As explained in Section 4.1, it was chosen to use generalised forces in this study, implying that the identified forces will account for excitations applied in any location. This is favorable in the sense that it considers the true load state as felt by the bridge in-operation, where multiple sources of excitation always are present. The drawback is that the wave forces cannot be studied separately, as the output data always will contain contributions from wind and traffic. We do still expect that the wave force is dominant, especially in the frequency range $2-4$ rad/s ($0.3-0.6$ Hz).

There are also uncertainties associated with the force reconstruction from wave data. Since no other information was available, it was assumed that the wave field is homogenous across the entire strait, meaning that the directional wave spectrum is the same at the seven pontoon locations. However, it cannot be ruled out that in reality, the wave field differs closer to land, for example, or that inhomogeneities can occur when waves approach from $\theta = 90°$ due to the islands north of the bridge (cf. Fig. 12).

In a stationary sea state, it is likely that the waves propagate from one dominant direction. However, it is not uncommon, in the EMEP estimation of $S_{\eta\eta}(\omega, \theta)$, for the spectral energy to bleed out in erroneous directions. For example, it is unlikely that waves will approach from directions close to 0 or 180 degrees, as large land masses are found at either end of the bridge. This can be seen in Fig. 15[..[22]]d, for example, where a minor peak occurs at $\theta = 180°$. The EMEP utilises the cross-spectral density between the different wave elevation measurements; how the cross-spectral density matrix is calculated can influence the estimation of $S_{\eta\eta}(\omega, \theta)$. We notice that the directional part of this function can be sensitive, but the frequency content is relatively stable. Errors in the wave directions in turn lead to errors in the estimated forces. Ideally, more than six wave radars should be used for a robust reconstruction, and the array of radars should extend both in the x- and y-direction, although at the Bergsøysund bridge, practical limitations restrict the number of feasible locations of the sensors. Since the transfer functions

[21] removed: small

[22] removed: c

$Q_i^{(m)}(\omega, \theta)$ originate from a pontoon model, which can be erroneous, the cross-spectral density from Eq. 37 will also be prone to model errors. However, it will not be highly sensitive to these model errors considering that the force reconstruction in Eq. 37 is not ill-posed in the same way as the inverse identification.

The narrow peaks that occur in the identified forces often indicate errors propagated from (state-space) model errors. However, it cannot be ruled out that some also stem from actual load phenomena. For example, the interaction between two pontoons through the fluid is a proximity effect that is not considered but can have a significant influence since the pontoon size is approximately 20×34 m and the centre-to-centre distance is 105 m. Interaction phenomena can give rise to peaks in the transfer functions $Q_i^{(m)}(\omega, \theta)$, for example, which could be mistaken for a resonant peak from the structure itself. The modelling of this interaction would be interesting to study but requires a multibody model of the pontoons, which is a problem that is highly costly to compute.

Inverse identification of forces could ideally be used to verify current load models and give insight into uncertain load mechanisms. Although these forces will relate to the specific structure, any new observations and accumulated experiences could be useful in future design of bridges, as predictions of the structural and environmental behavior (and related uncertainties) still often rely on reference data from existing structures. Overall, the reported uncertainties indicate that challenges are still faced in the robust application of the force identification methods to full-scale studies with high complexity. A reduction of these uncertainties by improvements in modelling, methodology or measurement data is necessary for more reliable force estimates.

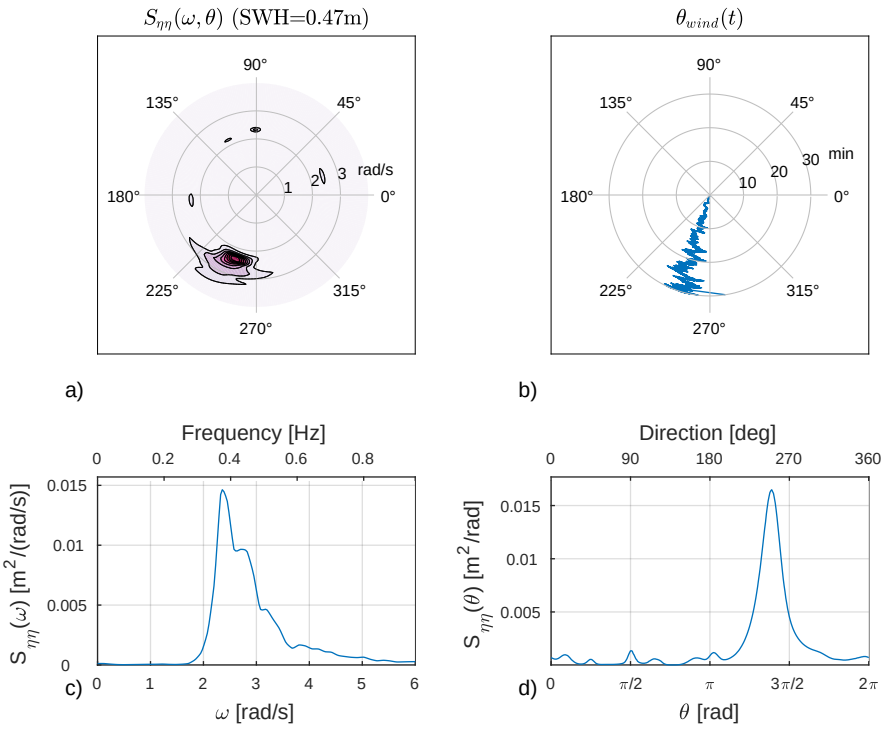

Figure 13: Ambient conditions of recording 1: (a) Estimated directional wave spectrum; (b) evolution of wind direction; (c) one-dimensional wave spectrum; (d) directional spectrum.

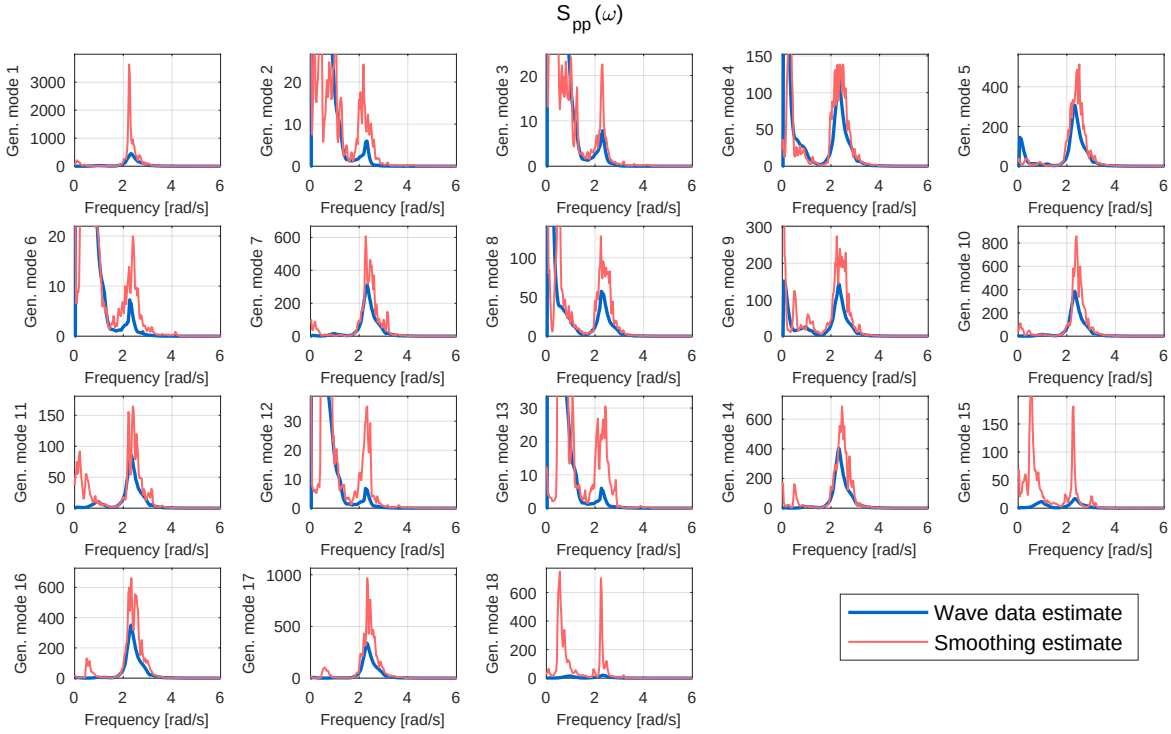

Figure 14: Diagonal elements of the PSD matrix $\mathbf{S}_{pp}(\omega)$ for the generalised forces in recording 1.

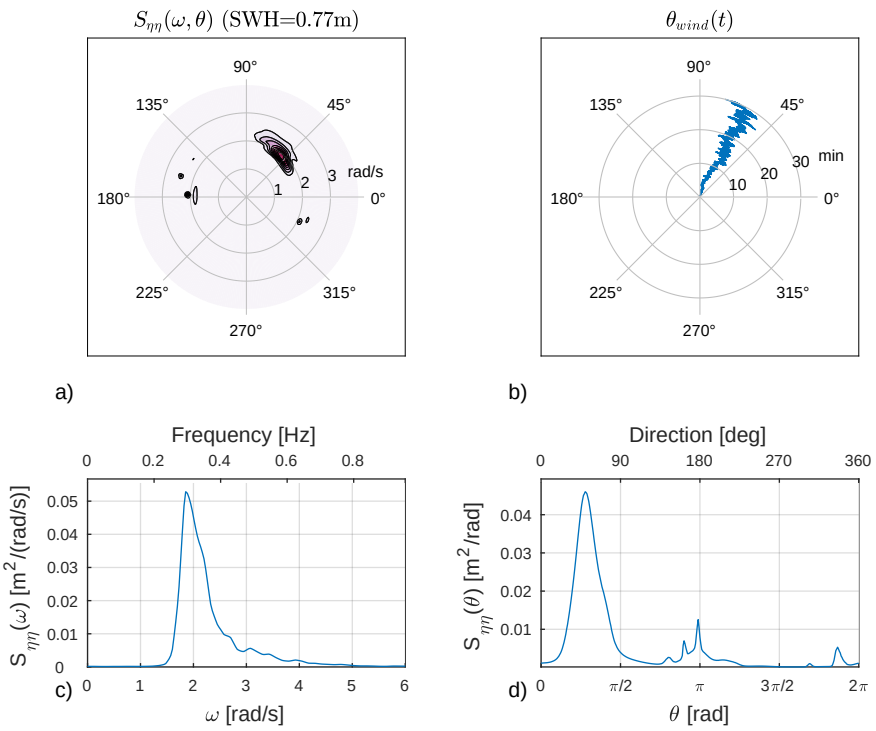

Figure 15: Ambient conditions of recording 2: (a) Estimated directional wave spectrum; (b) evolution of wind direction; (c) one-dimensional wave spectrum; (d) directional spectrum.

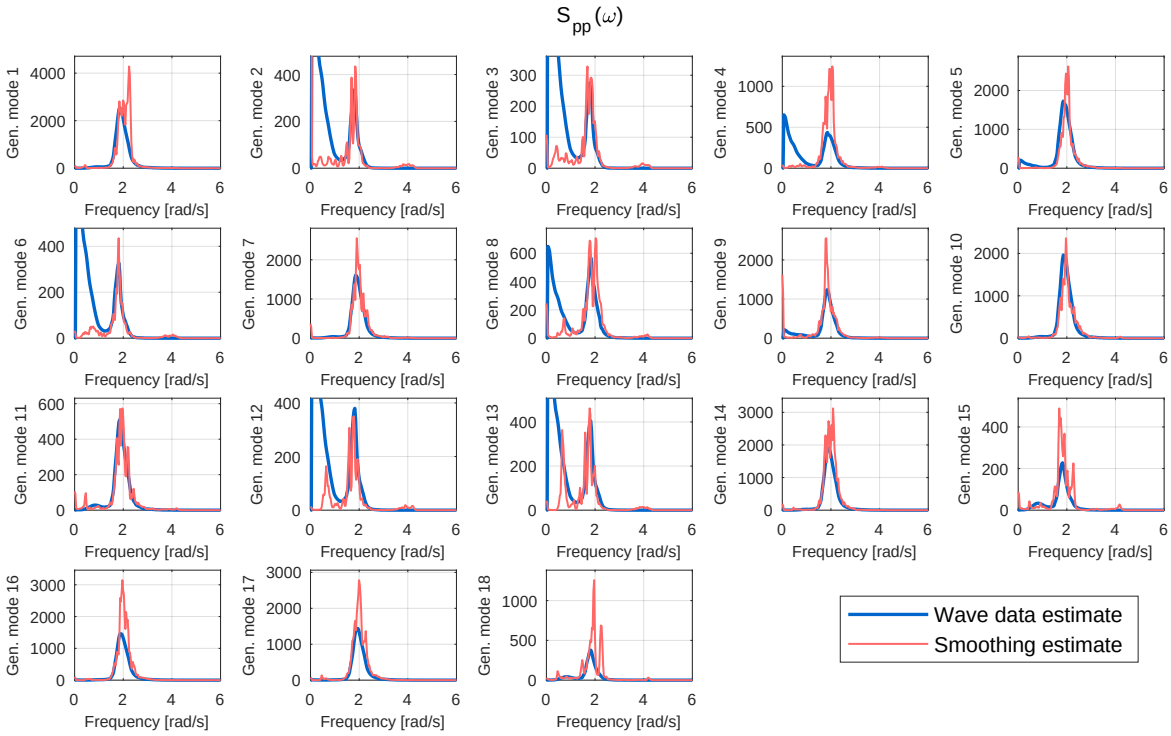

Figure 16: Diagonal elements of the PSD matrix $\mathbf{S}_{pp}(\omega)$ for the generalised forces in recording 2.

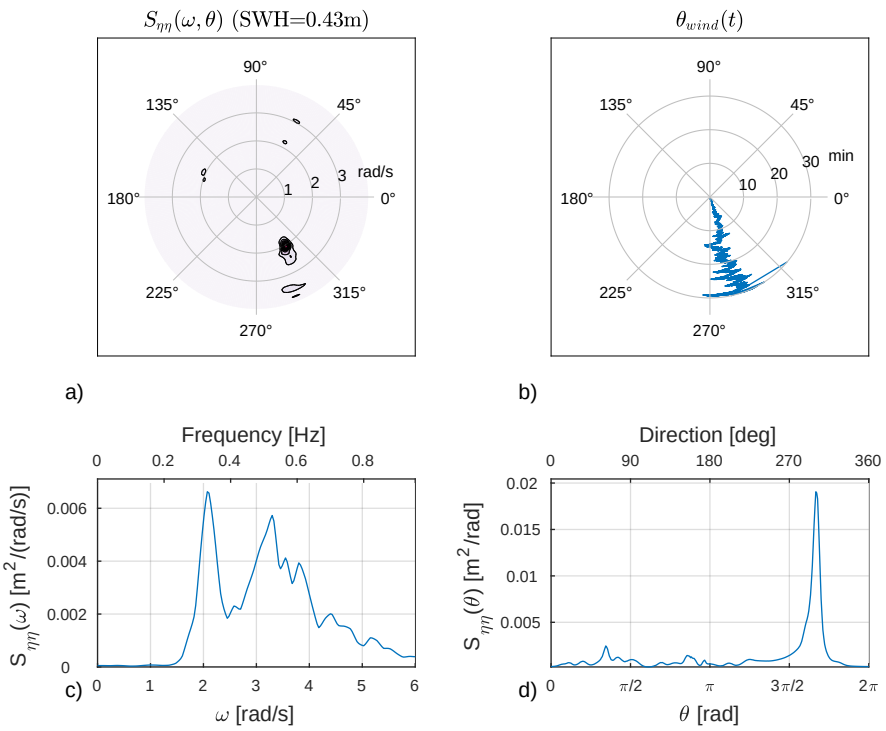

Figure 17: Ambient conditions of recording 3: (a) Estimated directional wave spectrum; (b) evolution of wind direction; (c) one-dimensional wave spectrum; (d) directional spectrum.

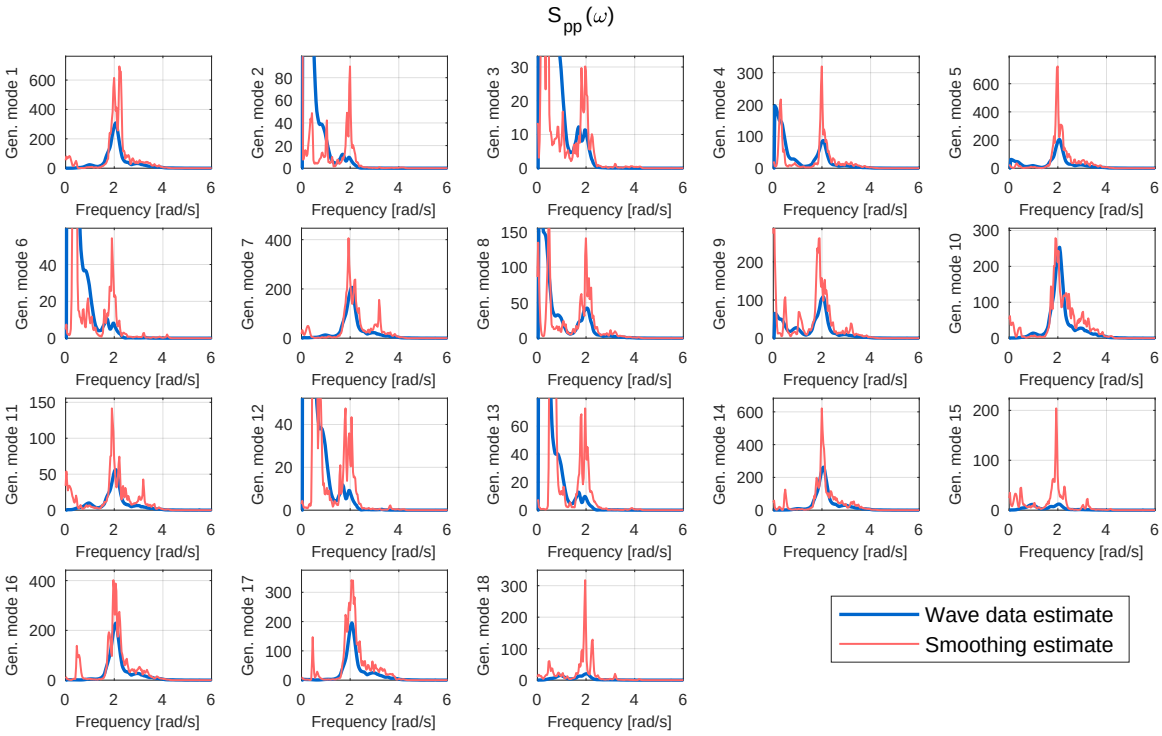

Figure 18: Diagonal elements of the PSD matrix $\mathbf{S}_{pp}(\omega)$ for the generalised forces in recording 3.

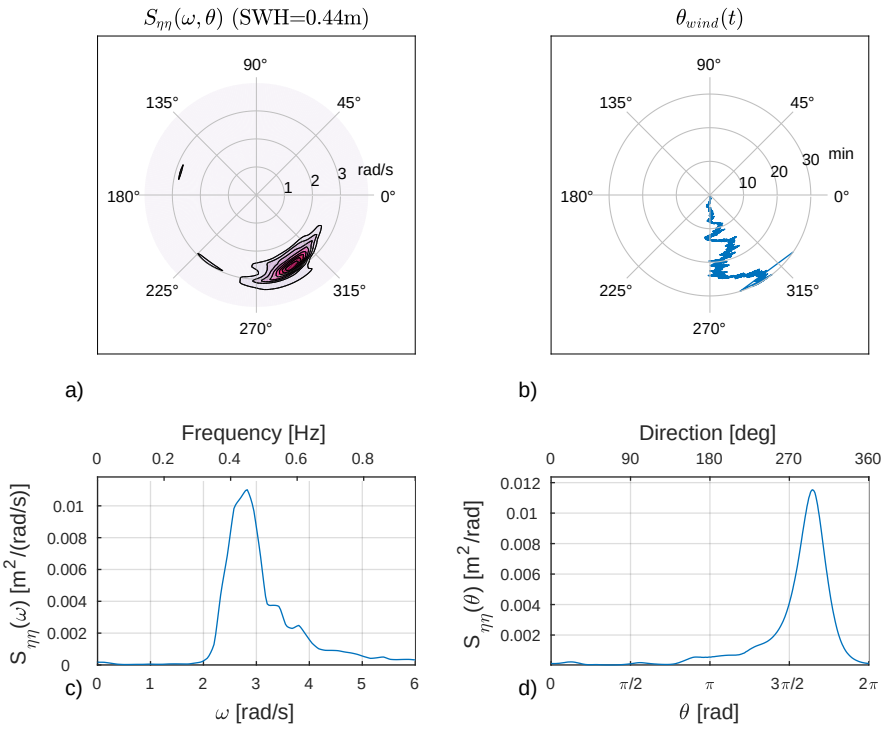

Figure 19: Ambient conditions of recording 4: (a) Estimated directional wave spectrum; (b) evolution of wind direction; (c) one-dimensional wave spectrum; (d) directional spectrum.

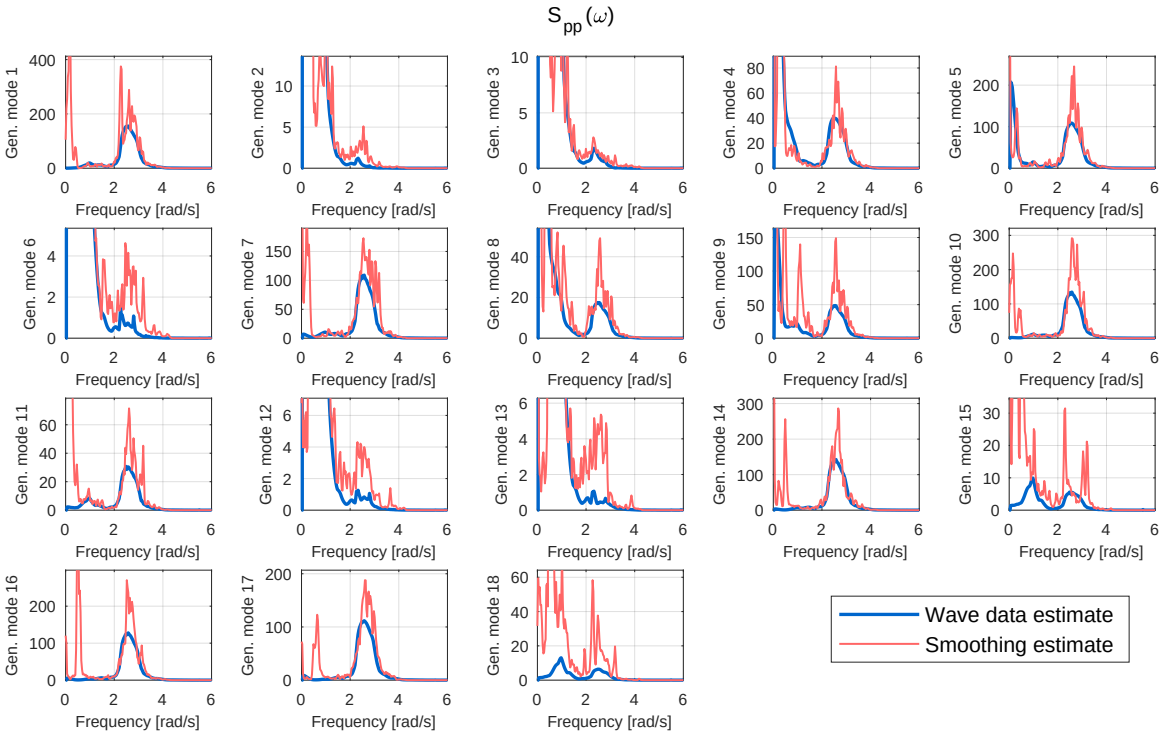

Figure 20: Diagonal elements of the PSD matrix $\mathbf{S}_{pp}(\omega)$ for the generalised forces in recording 4.

6. Conclusions

This paper presented a case study of the full-scale identification of the wave forces on the pontoons of the Bergsøysund bridge. Two approaches were used to assess the wave forces. The first is an application of inverse methods for force identification using measured acceleration data together with a high-fidelity numerical model of the structure. The second constructs the spectral density of the wave forces by combining the pontoon transfer functions for wave excitation and a directional wave spectrum estimated from six wave elevation measurements. A frequency-domain comparison of the force estimates from the two approaches indicated that the identified forces were reasonable. The discrepancies that were observed can be attributed to a number of significant uncertainties, such as model errors, sensor inaccuracies, pontoon interaction, and inhomogeneities in the wave field. However, a direct quantification of the force uncertainty is not yet attainable, and it remains unknown to what extent each of these sources of uncertainties influences the solution.

Acknowledgements

This research was conducted with financial support from the Norwegian Public Roads Administration. The authors gratefully acknowledge this support.

References

References

[1] J. Hwang, A. Kareem, H. Kim, Wind load identification using wind tunnel test data by inverse analysis, Journal of Wind Engineering and Industrial Aerodynamics 99 (2011) 18–26.

[2] L. Zhi, M. Fang, Q. Li, Estimation of wind loads on a tall building by an inverse method, Structural Control and Health Monitoring (2016).

[3] Y. Niu, C.-P. Fritzen, H. Jung, I. Buethe, Y.-Q. Ni, Y.-W. Wang, Online simultaneous reconstruction of wind load and structural responses: theory and application to Canton tower, Computer-Aided Civil and Infrastructure Engineering 30 (2015) 666–681.

[4] L. Zhi, Q. Li, M. Fang, Identification of wind loads and estimation of structural responses of super-tall buildings by an inverse method, Computer-Aided Civil and Infrastructure Engineering 31 (2016) 966–982.

[5] E. Lourens, E. Reynders, G. De Roeck, G. Degrande, G. Lombaert, An augmented Kalman filter for force identification in structural dynamics, Mechanical Systems and Signal Processing 27 (2012) 446–460.

[6] S. E. Azam, E. Chatzi, C. Papadimitriou, A dual Kalman filter approach for state estimation via output-only acceleration measurements, Mechanical Systems and Signal Processing 60 (2015) 866–886.

[7] E. Lourens, C. Papadimitriou, S. Gillijns, E. Reynders, G. De Roeck, G. Lombaert, Joint input-response estimation for structural systems based on reduced-order models and vibration data from a limited number of sensors, Mechanical Systems and Signal Processing 29 (2012) 310–327.

[8] K. Maes, A. Smyth, G. De Roeck, G. Lombaert, Joint input-state estimation in structural dynamics, Mechanical Systems and Signal Processing 70–71 (2016) 445–466.

[9] K. Maes, S. Gillijns, G. Lombaert, A smoothing algorithm for joint input-state estimation in structural dynamics, Mechanical Systems and Signal Processing 98 (2018) 292–309.

[10] T. S. Nord, E. Lourens, O. Øiseth, A. Metrikine, Model-based force and state estimation in experimental ice-induced vibrations by means of Kalman filtering, Cold Regions Science and Technology 111 (2015) 13–26.

[11] T. S. Nord, O. Øiseth, E. Lourens, Ice force identification on the Norströmsgrund lighthouse, Computers & Structures 169 (2016) 24–39.

[12] Z. Cheng, Z. Gao, T. Moan, Hydrodynamic load modeling and analysis of a floating bridge in homogeneous wave conditions, Marine Structures 59 (2018) 122–141.

[13] Y. Xu, O. Øiseth, T. Moan, Time domain simulations of wind-and wave-induced load effects on a three-span suspension bridge with two floating pylons, Marine Structures 58 (2018) 434–452.

[14] Z. Cheng, Z. Gao, T. Moan, Wave load effect analysis of a floating bridge in a fjord considering inhomogeneous wave conditions, Engineering Structures 163 (2018) 197–214.

[15] K. Unneland, Identification and order reduction of radiation force models of marine structures, Ph.D. thesis, Norwegian University of Science and Technology - Faculty of Information Technology, Mathematics and Electrical Engineering, 2007.

[16] R. Taghipour, T. Perez, T. Moan, Hybrid frequency–time domain models for dynamic response analysis of marine structures, Ocean Engineering 35 (2008) 685–705.

[17] R. Taghipour, T. Perez, T. Moan, Time-domain hydroelastic analysis of a flexible marine structure using state-space models, Journal of Offshore Mechanics and Arctic Engineering 131 (2009) 011603.

[18] E. Kristiansen, Å. Hjulstad, O. Egeland, State-space representation of radiation forces in time-domain vessel models, Ocean Engineering 32 (2005) 2195–2216.

[19] T. Pérez, T. I. Fossen, Time-vs. frequency-domain identification of parametric radiation force models for marine structures at zero speed, Modeling, Identification and Control 29 (2008) 1–19.

[20] K. A. Kvåle, R. Sigbjörnsson, O. Øiseth, Modelling the stochastic dynamic behaviour of a pontoon bridge: A case study, Computers & Structures 165 (2016) 123–135.

[21] Ø. W. Petersen, O. Øiseth, T. S. Nord, E. Lourens, Estimation of the full-field dynamic response of a floating bridge using Kalman-type filtering algorithms, Mechanical Systems and Signal Processing 107 (2018) 12–28.

[22] K. Roger, Airplane math modelling methods for active control design, in: Structural Aspects of Control, AGARD Conference Proceedings, volume 9, 1977, pp. 4.1–4.11.

[23] X. Chen, M. Matsumoto, A. Kareem, Time domain flutter and buffeting response analysis of bridges, Journal of Engineering Mechanics 126 (2000) 7–16.

[24] O. Øiseth, A. Rönnquist, R. Sigbjörnsson, Finite element formulation of the self-excited forces for time-domain assessment of wind-induced dynamic response and flutter stability limit of cable-supported bridges, Finite Elements in Analysis and Design 50 (2012) 173–183.

[25] K. A. Kvåle, O. Øiseth, Structural monitoring of an end-supported pontoon bridge, Marine Structures 52 (2017) 188–207.

[26] K. A. Kvåle, O. Øiseth, A. Rønnquist, Operational modal analysis of an end-supported pontoon bridge, Engineering Structures 148 (2017) 410–423.

[27] Ø. W. Petersen, O. Øiseth, T. S. Nord, E. Lourens, Model-based estimation of hydrodynamic forces on the Bergsoysund Bridge, in: Proceedings of the 34th IMAC, A Conference and Exposition on Structural Dynamics, Dynamics of Civil Structures, Volume 2, Springer, 2016, pp. 217–228.

[28] K. Maes, E. Lourens, K. Van Nimmen, E. Reynders, G. De Roeck, G. Lombaert, Design of sensor networks for instantaneous inversion of modally reduced order models in structural dynamics, Mechanical Systems and Signal Processing 52 (2014) 628–644.

[29] K. Kvåle, O. Øiseth, Characterization of the wave field around an existing end-supported pontoon bridge from simulated data, in: Proceedings of The International Conference on Earthquake engineering and Structural Dynamics 2017 (ICESD2017), 2017.

[30] D. Johnson, DIWASP, a directional wave spectra toolbox for matlab: User manual, Research Report WP-1601-DJ (V1.1), Centre for Water Research, University of Western Australia, 2012.

[31] N. Hashimoto, T. Nagai, T. Asai, Extension of the maximum entropy principle method for directional wave spectrum estimation, in: B. L. Edge (Ed.), Proceedings of 24th Conference on Coastal Engineering, 1994, pp. 232–246.

[32] F. G. Giske, B. J. Leira, O. Øiseth, Efficient computation of cross-spectral densities in the stochastic modelling of waves and wave loads, Applied Ocean Research 62 (2017) 70–88.